Microscopic Inner Retinal Hyper-Reflective Phenotypes in Retinal and Neurologic Disease

Drew Scoles,[1] Brian P. Higgins,[2] Robert F. Cooper,[3] Adam M. Dubis,[4,5] Phyllis Summerfelt,[2] David V. Weinberg,[2] Judy E. Kim,[2] Kimberly E. Stepien,[2] Joseph Carroll,[2,3,6,7] and Alfredo Dubra[2,3,7]

[1]Department of Biomedical Engineering, University of Rochester, Rochester, New York, United States
[2]Department of Ophthalmology, Medical College of Wisconsin, Milwaukee, Wisconsin, United States
[3]Department of Biomedical Engineering, Marquette University, Milwaukee, Wisconsin, United States
[4]Moorfields Eye Hospital, London, United Kingdom
[5]Institute of Ophthalmology, University College London, London, United Kingdom
[6]Department of Cell Biology, Neurobiology and Anatomy, Medical College of Wisconsin, Milwaukee, Wisconsin, United States
[7]Department of Biophysics, Medical College of Wisconsin, Milwaukee, Wisconsin, United States

Correspondence: Joseph Carroll, The Eye Institute, Medical College of Wisconsin, 925 N 87th Street, Milwaukee, WI 53226; jcarroll@mcw.edu.
Alfredo Dubra, The Eye Institute, Medical College of Wisconsin, 925 N 87th Street, Milwaukee, WI 53226; adubra@mcw.edu.

Submitted: April 26, 2014
Accepted: May 21, 2014

Citation: Scoles D, Higgins BP, Cooper RF, et al. Microscopic inner retinal hyper-reflective phenotypes in retinal and neurologic disease. *Invest Ophthalmol Vis Sci*. 2014;55:4015–4029. DOI:10.1167/iovs.14-14668

Purpose. We surveyed inner retinal microscopic features in retinal and neurologic disease using a reflectance confocal adaptive optics scanning light ophthalmoscope (AOSLO).

Methods. Inner retinal images from 101 subjects affected by one of 38 retinal or neurologic conditions and 11 subjects with no known eye disease were examined for the presence of hyper-reflective features other than vasculature, retinal nerve fiber layer, and foveal pit reflex. The hyper-reflective features in the AOSLO images were grouped based on size, location, and subjective texture. Clinical imaging, including optical coherence tomography (OCT), scanning laser ophthalmoscopy, and fundus photography was analyzed for comparison.

Results. Seven categories of hyper-reflective inner retinal structures were identified, namely punctate reflectivity, nummular (disc-shaped) reflectivity, granular membrane, waxy membrane, vessel-associated membrane, microcysts, and striate reflectivity. Punctate and nummular reflectivity also was found commonly in normal volunteers, but the features in the remaining five categories were found only in subjects with retinal or neurologic disease. Some of the features were found to change substantially between follow up imaging months apart.

Conclusions. Confocal reflectance AOSLO imaging revealed a diverse spectrum of normal and pathologic hyper-reflective inner and epiretinal features, some of which were previously unreported. Notably, these features were not disease-specific, suggesting that they might correspond to common mechanisms of degeneration or repair in pathologic states. Although prospective studies with larger and better characterized populations, along with imaging of more extensive retinal areas are needed, the hyper-reflective structures reported here could be used as disease biomarkers, provided their specificity is studied further.

Keywords: adaptive optics, inner retina, ophthalmoscopy, neuro-ophthalmology, retinal disease

Since the first demonstration of adaptive optics (AO) for retinal imaging,[1] its main application has been the study of the cone photoreceptors by taking advantage of their strongly directional reflectivity (waveguiding).[2] Defects in a structural protein,[3] membrane channel,[4–6] physical disruption of the photoreceptor,[7] or otherwise,[8,9] can show as abnormal reflectivity patterns and often result in decreased or complete absence of reflectivity (dark cone). Although each independent study has improved the understanding of a particular disease, when the collective findings are considered together it becomes clear that impaired cone photoreceptor waveguiding is an important, yet nonspecific biomarker for photoreceptor integrity.[10]

Adaptive optics imaging also is being used to study retinal microvasculature structure and perfusion in normal and diseased eyes,[11–23] with a recent focus on microaneurysms.[21,22] Studies on diabetic retinopathy and other conditions[13,20,21] have found that microscopic vascular changes and, in particular, microaneurysm morphology, also are not specific to any one disease.[22] As with the dark cone phenotype, microscopic vascular pathology, therefore, may be more suggestive of common response mechanisms, rather than disease-specific insults.

With the exception of recent work,[24–28] inner retinal pathology remains largely unexplored with AO ophthalmoscopy. However, previous imaging by us (Scoles DH, et al. *IOVS* 2012;53:ARVO E-Abstract 6957; Scoles DH, et al. *IOVS* 2013;54:ARVO E-Abstract 1434) and others (Gast TJ, et al. *IOVS* 2013;54:ARVO E-Abstract 1507) performed in a small number of subjects seem to suggest that abnormal epiretinal highly-reflective structures also are not disease-specific.

Table. Retinal Diseases and Phenotypes Observed in this Study

Pathology, *n*	A	B	C	D	E	F	G
Achromatopsia, 5	X	X	X				
Acquired optic disc pit, 1	X		X	X			
Acute macular neuroretinopathy, 1							X
AMD, 2			X	X			
Astrocytic hamartoma, 1			X		X		X
Autoimmune retinopathy, 1			X				
Best disease, 2	X					X	X
Birdshot choroidoretinopathy, 4	X		X	X			
Bornholm eye disease, 1	X						
BRAO & BRVO, 3	X	X	X				
Central retinal artery occlusion, 1	X			X			
Central serous retinopathy, 3	X	X	X	X	X		X
Choroideremia, 8	X			X	X		X
Color blindness, 1	X	X					
Commotio retinae, 5	X	X				X	X
Cone dystrophy, 4	X		X	X			X
Cotton-wool spot, 1		X					
Diabetic retinopathy, 2	X	X			X		
Epiretinal membrane, 2		X	X				
Free of disease, 11	X	X		X			
Glaucoma, 11	X	X	X	X			
Leber's congenital amaurosis, 2	X			X	X		
Leber's hereditary optic neuropathy, 1	X	X					
Macular hole, 4	X	X	X	X	X	X	
Macular telangiectasia, 7	X		X		X	X	
Microscotoma, 3	X	X	X				
Multiple sclerosis, 1	X	X					
Optic atrophy, 5	X	X	X	X	X	X	
Optic nerve drusen, 2		X					
Optic neuritis, 3						X	
Parkinson's disease, 3	X	X	X	X	X		X
Pathologic myopia, 1				X			
Premature birth, 1	X						
Retinitis pigmentosa, 4	X	X	X	X	X		
Retinoschisis, 1		X				X	X
Rubella retinopathy, 1	X		X		X		
Stargardt, 1					X		
Traumatic brain injury, 1						X	
Unknown retinopathy, 1		X					X

The columns represent each of the seven findings described here; an "X" indicates that it was observed in our cohort. The absence of a feature (no "X") should not be interpreted as an absolute absence, rather not yet observed. A, punctate reflectivity; B, nummular (disc-shaped) reflectivity; C, granular membrane; D, waxy membrane; E, vessel associated membrane; F, microcysts; G, striate reflectivity.

In the present study, we sought to expand upon previous work by reexamining inner retinal (anterior to the outer plexiform layer) and epiretinal (anterior to the inner limiting membrane) findings in AO scanning light ophthalmoscopic (AOSLO) imaging across a broad cohort of retinal and neurologic diseases. The superior transverse image resolution of the AOSLO relative to non-AO ophthalmoscopes revealed previously unreported hyper-reflective structures (relative to their surroundings). The results of this study also indicated that, similar to the biomarkers of photoreceptor and vascular diseases, microscopic and macroscopic hyper-reflective inner retinal features are not unique to a single condition. Although the findings described here may not be disease-specific, their potential for aiding diagnosing, monitoring disease progression, and adjusting management remains to be determined. In what follows, the appearance of similar inner retinal features across varied conditions is shown, followed by specific examples highlighting each feature and placing the AOSLO findings in the context of fundus photography, scanning laser ophthalmoscopy, and en face OCT sections.

Methods

Subjects

Research procedures followed the tenets of the Declaration of Helsinki, and informed written consent was obtained from all subjects after explanation of the nature and possible consequences of the study. The study protocol was approved by the institutional review board at the Medical College of Wisconsin and the University of Rochester. Subjects were either referred by their physicians, or self-referred in response to advertised studies.

Axial length measurements were obtained on all subjects (Zeiss IOL Master; Carl Zeiss Meditec, Dublin, CA, USA). Using the Gullstrand 2 schematic eye, the predicted 291 μm per degree of visual angle[29] was scaled linearly by the subject's axial length to determine the scale of AOSLO images. Before all retinal imaging, the eyes to be imaged were dilated and cycloplegia was induced through topical application of phenylephrine hydrochloride (2.5%) and tropicamide (1%).

Investigative Ophthalmology & Visual Science

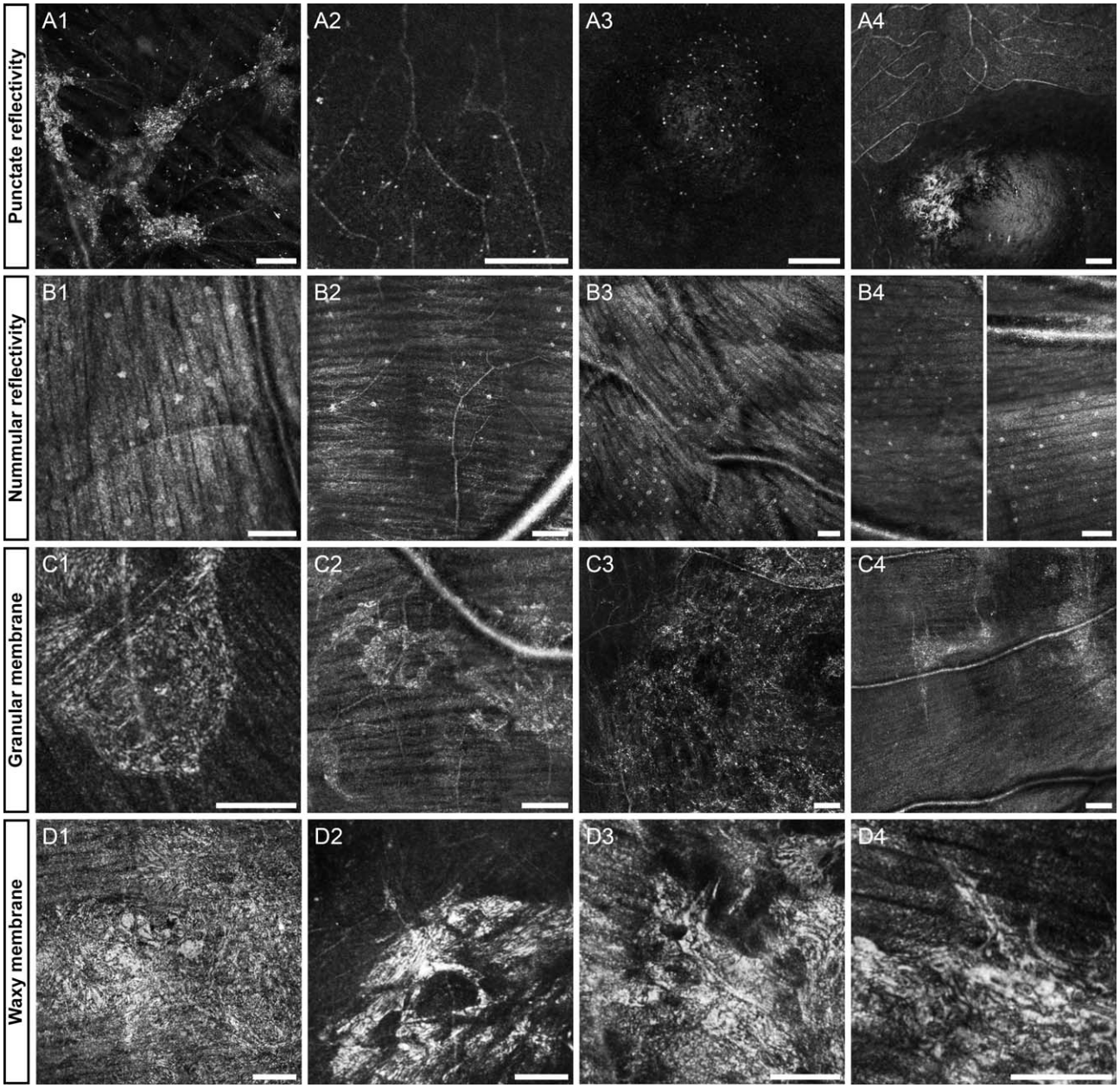

Figure 1. Representative images of the first four features: punctate reflectivity (**A1–4**), nummular reflectivity (**B1–4**), granular membrane (**C1–4**), waxy reflectivity (**D1–4**). Diseases in each group include, rubella retinopathy (**A1**), achromatopsia (**A2**), optic disk pit (**A3**), normal (**A4**), normal (**B1**), glaucoma (**B2**), normal (**B3**), multiple sclerosis (**B4**), diabetic retinopathy (**C1**), Parkinson's (**C2**), branch retinal vein occlusion (**C3**), optic atrophy (**C4**), cone dystrophy (**D1**), central serous retinopathy (**D2**), birdshot choroidoretinopathy (**D3**), age-related macular degeneration (AMD, [**D4**]). (**B4**) is a contiguous vertical montage split into two halves, top is on the *left* and bottom is on the *right*. The *first column* of each row is highlighted below in Figures 3, 5, 7, 9. S*cale bars*: 100 μm.

Optical Coherence Tomography

In all subjects, spectral domain-optical coherence tomography (SD-OCT) line scans and cube scans were performed in the area of AOSLO imaging (Carl Zeiss Meditec; Bioptigen, Research Triangle Park, NC, USA; Heidelberg Engineering, Heidelberg, Germany). Dense SD-OCT volumes also were obtained (Bioptigen), nominally covering 3 × 3 (400 A-scans/B-scans; 400 B-scans) or 7 × 7 (1000 A-scans/B-scans; 250 B-scans) mm, and used to create en face OCT sections approximately 50 μm thick at the retinal layer(s) of interest with custom software (Java; Oracle, Redwood City, CA, USA). The OCT B-scans through features of interest shown below were generated by registering and averaging 3 adjacent B-scans to increase signal-to-noise ratio.[30] All OCT images are displayed in logarithmic scale. The fundus image provided by the line scan ophthalmoscope (LSO; Carl Zeiss Meditec) was recorded for comparison and registration of AOSLO images.

Confocal Reflectance Adaptive Optics Retinal Imaging

Inner retinal AOSLO images from 101 subjects representing 38 different retinal conditions (see Table for full list included in this study), acquired between August 2010 and February 2014 were identified. All images were collected using 680 or 790 nm

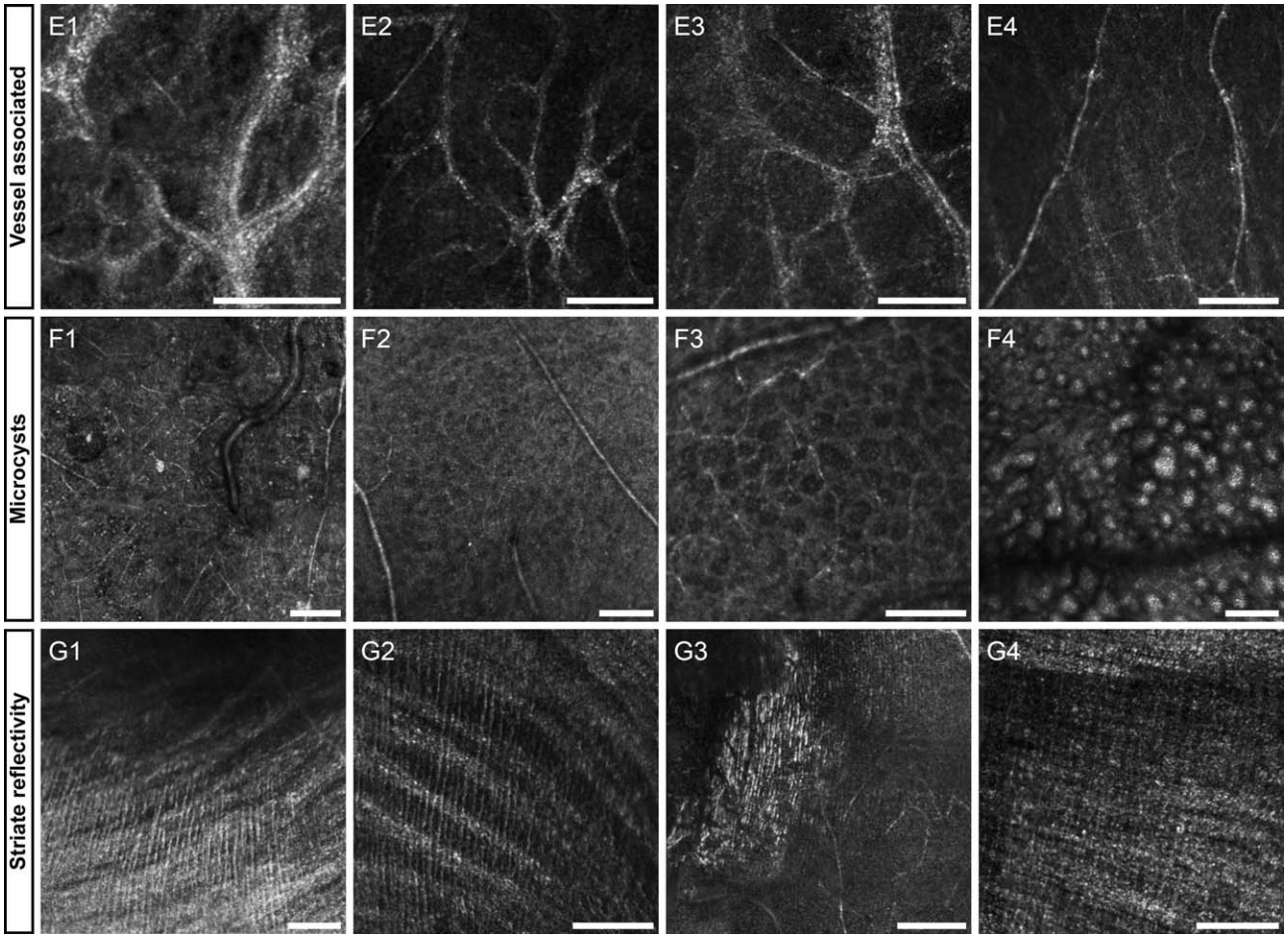

Figure 2. Representative images of the final three features: vessel-associated membrane (**E1-4**), microcysts (**F1–4**), striate reflectivity (**G1–4**). Diseases in each group include Leber's congenital amaurosis (**E1**), Stargardt's (**E2**), macular hole (**E3**), diabetic retinopathy (**E4**), macular telangiectasia (**F1**), glaucoma (**F2**), optic neuritis (**F3**), optic atrophy (focused on photoreceptors) (**F4**), Best's disease (**G1**), choroideremia (**G2**), commotio retinae (**G3**), unknown retinopathy (**G4**). The *first column* of each row is highlighted below in Figures 12, 13, 15. *Scale bars*: 100 μm.

superluminescent diodes (Superlum, Cork, Ireland), on one of three similar custom built AOSLO instruments at the University of Rochester and the Medical College of Wisconsin.[31] Incident powers measured at the cornea were 15 to 30 μW for a 850-nm wavefront sensing light source, 120 μW for the 680-nm source and 80 to 150 μW for the 790-nm source. All exposures were kept 5 times below the maximum permissible exposure as per ANSI Z136.1.[32,33] Inner retinal images from 11 subjects with no history of vision-limiting eye disease also were analyzed for comparison. Where possible, images from subjects imaged on multiple occasions were compared to display longitudinal changes of inner retinal features. The AOSLOs were focused on the retinal features of interest by changing the curvature of the deformable mirror (Hi-Speed DM97-15; Alpao, Giéres, France). A 1 to 2 Airy disk confocal pinhole was used to provide axial sectioning and increase the contrast of structures of interest.[34] After the features were located and in focus, image sequences of 150 frames were captured at 17 frames per second. The images within each sequence were registered, and the 20 to 50 images with highest normalized cross-correlation relative to a user-selected reference frame were averaged to create a high signal-to-noise ratio result with minimal distortion due to eye motion.[35] Where possible, multiple registered images were tiled manually using Adobe Photoshop (Adobe Systems, Inc., Mountain View, CA, USA) to increase retinal coverage and/or to locate the feature with the context of fundus or OCT images. All AOSLO images are displayed in linear scale.

Results

Classification of Inner Retinal Phenotypes

The review of the hyper-reflective structures with consideration of previous work, as well as feature size, location and subjective perceived texture in the AOSLO images suggested seven classifications. We propose the following names for these findings: punctate reflectivity, nummular (disc-shaped) reflectivity, granular membrane, waxy membrane, vessel-associated membrane, microcysts, and striate reflectivity (Figs. 1, 2). For each disease included in this study, all images were examined for the presence of characteristics of any of the seven feature groups, with the results summarized in the Table. Given the limited retinal coverage in the AOSLO imaging protocols used, it is important to note that the absence of observation on this study does not mean the absence of a structure. In fact, it is very likely that future high-resolution retinal imaging studies on the conditions reported here will find features of more types than those encountered in this study. For this reason, it would be unreasonable to report prevalence of features within each condition without a larger population and more systematic study.

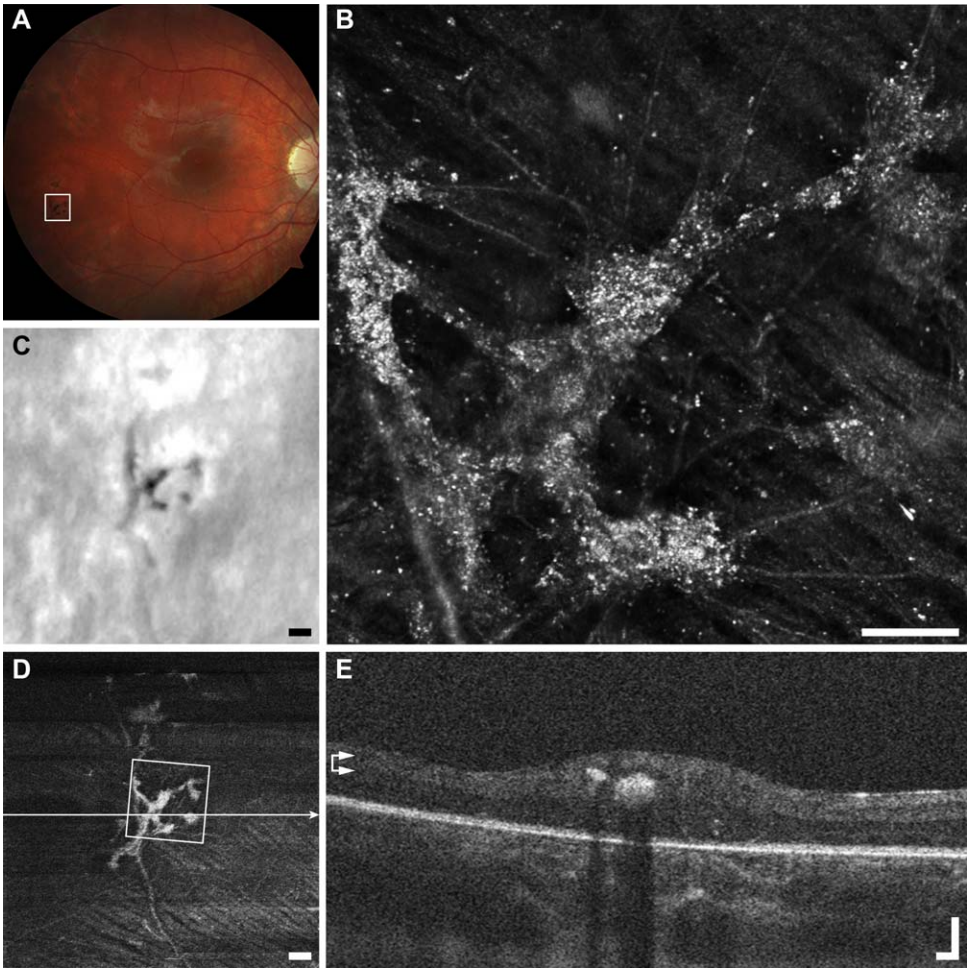

Figure 3. Multimodal imaging of punctate retinopathy example (**A1**), rubella retinopathy JC_0830. (**A**) Fundus photo with outline of AOSLO imaging. (**B**) The AOSLO image showing many small punctate reflective structures approximately 5 μm across. These structures appear to coalesce at the vessel creating what appears to be a membrane in (**C**, **D**). *Scale bar*: 100 μm. Of interest here are the small structures themselves, as they are found in a variety of other diseases and normal (Figs. 1A2–A4). (**C**) Fundus image from scanning laser ophthalmoscope (SLO) of the Cirrus OCT. *Scale bar*: 200 μm. (**D**) En face OCT segmented at the level of the vasculature (*horizontal arrows*). *Square* shows AOSLO imaging region of interest, *horizontal line* indicates location of OCT B-scan in (**E**). *Scale bar*: 200 μm. (**E**) OCT B-scan showing hyper-reflectivity surrounding a retinal vessel. *Scale bar*: 100 μm.

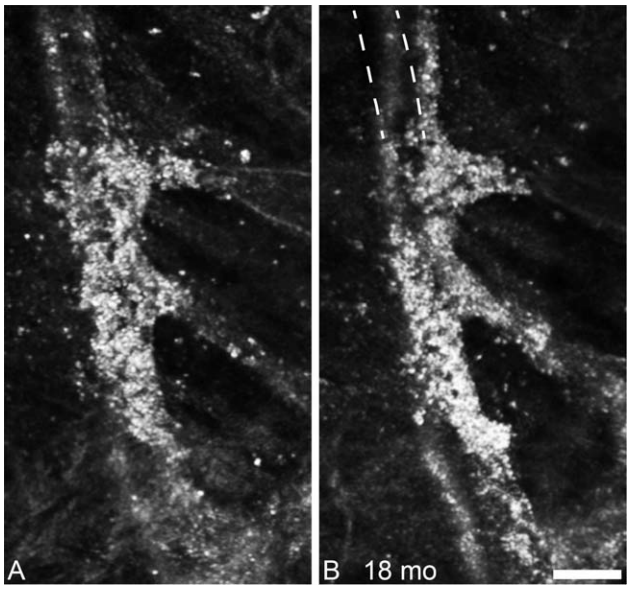

Punctate Reflectivity

In many diseases, as well as subjects free-of-disease who were imaged, sparse punctate reflective structures measuring approximately 3 to 5 μm in diameter (size can vary with image saturation) sometimes are visible on the inner surface of the retina. In normal volunteers, especially those aged 30 years old or more, these punctate reflective structures appear to line the inner surface of the foveal pit (Figs. 1A3, 1A4). Nearly identical features are observed in and around lesions on the inner surface of the retina or just deep in the ganglion cell layer (Figs. 1A1, 1A2) in subjects with rubella retinopathy and achromatopsia. It is unlikely that these features are cell somas (bodies), given their small size. It is possible, however, that

Figure 4. Follow-up of punctate hyper-reflectivity, an enlarged portion of the lesion shown in Figure 3. In the 18 months between the first imaging session (**A**), and the second imaging session there are few, if any, punctate structures that have not changed position. The lesion appears to be enlarging along the vessels, and contracting, such that the vessel no longer follows its original course, as illustrated by the dashed lines in (**B**). *Scale bar*: 50 μm.

Investigative Ophthalmology & Visual Science

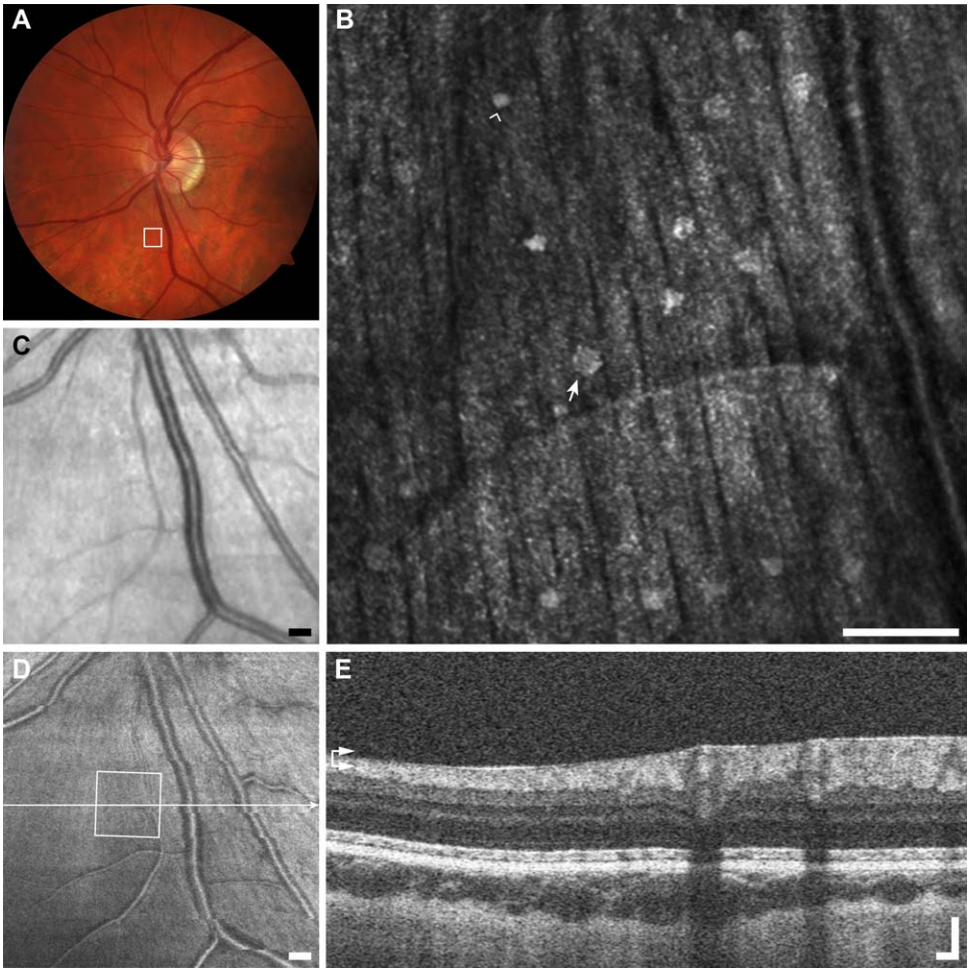

Figure 5. Multimodal imaging of nummular reflectivity example (**B1**), normal subject JC_0007. (**A**) Fundus photo with outline of AOSLO imaging. (**B**) The AOSLO image showing many reflective structures 10 to 30 μm across glistening on the surface of the NFL. *Scale bar*: 100 μm. In this image the largest dot is approximately 24 μm in diameter (*arrow*), and the smallest is only 13 μm (*arrowhead*). (**C**) The LSO fundus image does not resolve the dots. *Scale bar*: 200 μm. (**D**) En face OCT segmented at the level of the ILM (*horizontal arrows*) also cannot resolve dots. *Scale bar*: 200 μm. (**E**) The OCT B-scan does not clearly resolve the small dots. *Scale bar*: 100 μm.

they represent debris, or portions of cells. Due to the small size of these features, it is not possible to make any distinctions between those found in normal versus those found in pathology with current reflectance confocal AOSLO.

In the case highlighted (Fig. 3), the punctate features are thought to be collections of intra- or extracellular melanin granules.[36] This lesion appears dark brown or black in color fundus photography, suggesting that it may have been formed by pigment migration. Melanin granules are normally 1 to 1.2 μm in diameter,[37] which is below the theoretical Rayleigh resolution limit of 2.2 μm for 790-nm light and a 7.75-mm AOSLO pupil. This means that any structure 2.2 μm or smaller, such as melanin granules, will appear in the AOSLO images as 2.2 μm or larger, depending on object size, focus, and image saturation. The average diameter of each punctate feature was 3.5 ± 0.3 μm (mean ± SD, $n = 51$, Fig. 3), which is consistent with the expected theoretical size of a melanin granule as seen in our AOSLO (calculated as the convolution of the granule image with the object point spread function). The aggregation of punctate hyper-reflective features can span areas greater than 0.1 mm^2, in close association with a retinal vessel, with sparse individual or small clusters of hyper-reflective puncta observed in the surrounding region. Figure 3 highlights the discrepancy between imaging modalities potentially due to the detection methods, imaging wavelength and magnification, while the pigmented lesion appears dark in fundus photography and LSO, in en face OCT and AOSLO it appears hyper-reflective. Although the punctate structures in the foveal pit do

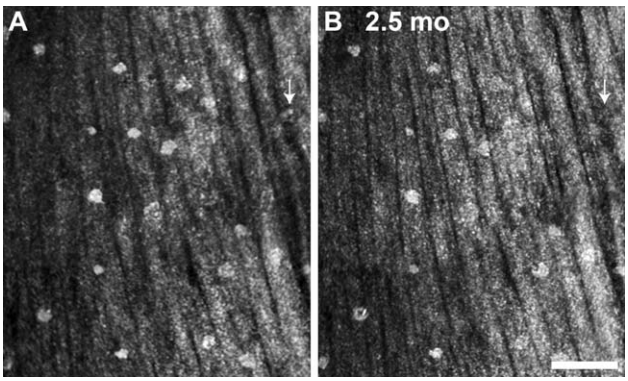

Figure 6. AOSLO follow-up imaging of nummular reflectivity in (**B1**), normal subject JC_0007. (**A**) Initial imaging. (**B**) A 2.5 month imaging reveals that nearly all of the dots have not moved or changed in appearance. *Arrows* depict a dot that was identified initially but not in follow-up. *Scale bar*: 100 μm.

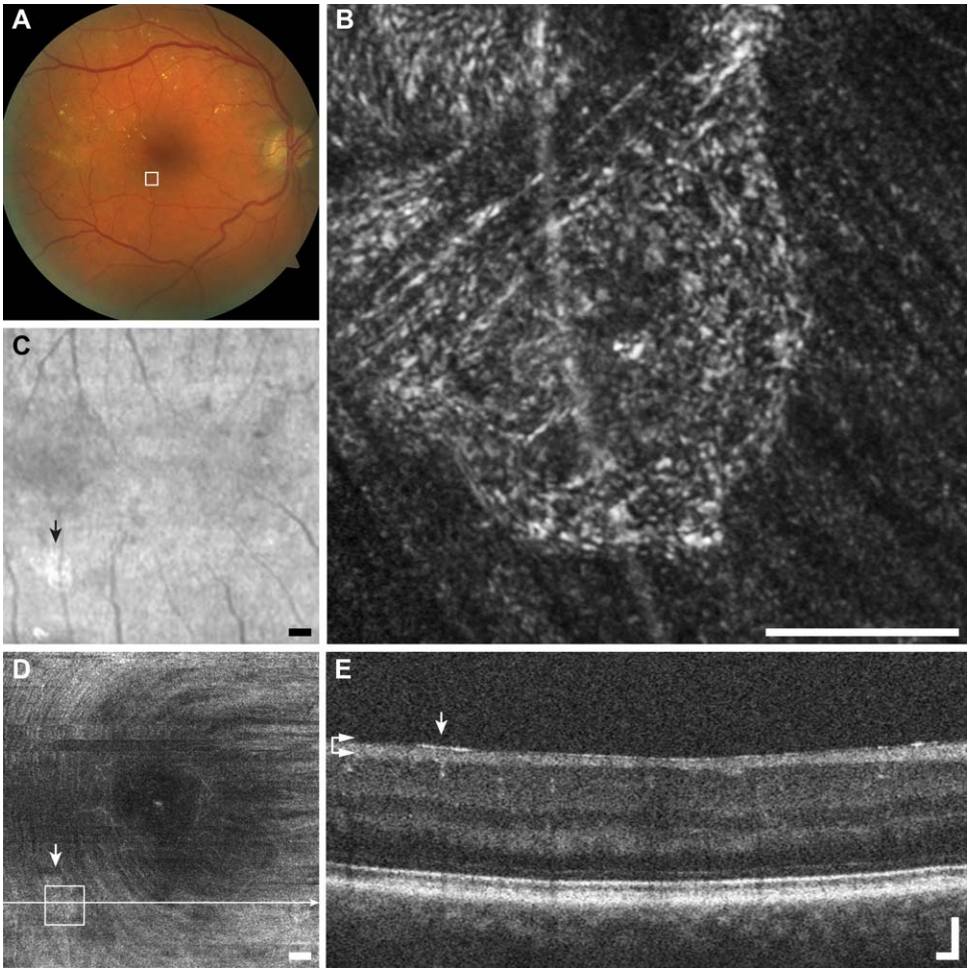

Figure 7. Multimodal imaging of granular membrane example (**C1**), diabetic retinopathy RS_1007. (**A**) Fundus photo with outline of AOSLO imaging does not reveal any membrane. (**B**) The AOSLO image shows a meshwork of small reflective granules, although highly reflective, the retinal vessel is clearly visible underneath. *Scale bar*: 100 μm. (**C**) The SLO fundus image shows a glistening membrane (arrow). *Scale bar*: 200 μm. (**D**) En face OCT segmented at the level of the ILM (*horizontal arrows*) also resolves the thin membrane (*arrow*). *Scale bar*: 200 μm. (**E**) The OCT B-scan shows a small glistening reflection on the surface of the NFL (*arrow*). *Scale bar*: 100 μm.

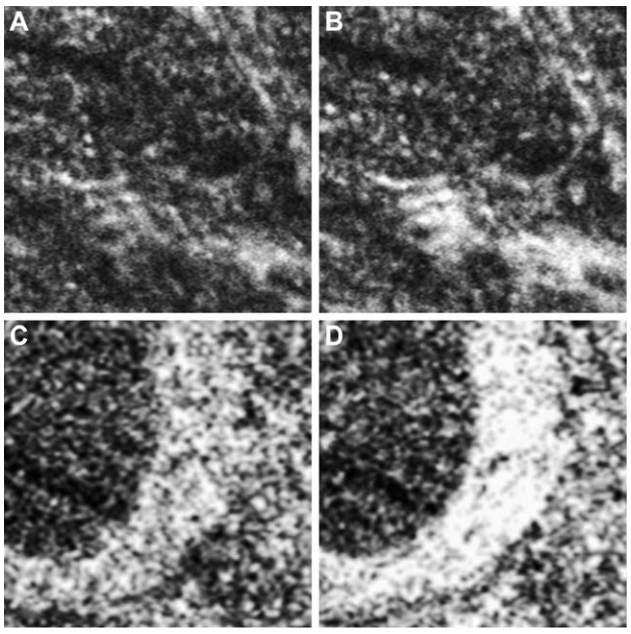

not appear to change noticeably over the duration of this study, the lesion in Figure 3 changed substantially over the 18 months between imaging sessions, with apparent reorganization of the punctate features inside and outside of the lesion (Fig. 4).

Nummular Reflectivity

In addition to the small punctate hyper-reflective features, there also are substantially larger (approximately 10–30 μm in diameter), round hyper-reflective features sometimes visible on the internal limiting membrane (ILM). Each spot has a granular texture nearly identical to that of the nerve fiber layer (NFL) below, and some have a circular clearing near their center.

Figure 8. Illustration of how the specular reflectivity of waxy membranes can lead to dramatic image intensity changes relative to the surrounding structures with eye motion. (**A**, **B**) are single frames taken from the same image sequence in subject KS_0625 with cone rod dystrophy (Fig. 1D4). The relative brightness of the membrane (*lower right*) changes substantially due to an 80-μm retinal movement. An example from subject DLAB_0029 with glaucoma shows a similar phenomenon caused by a 52-μm retinal movement (**C**, **D**). Each panel is 100 μm across.

Investigative Ophthalmology & Visual Science

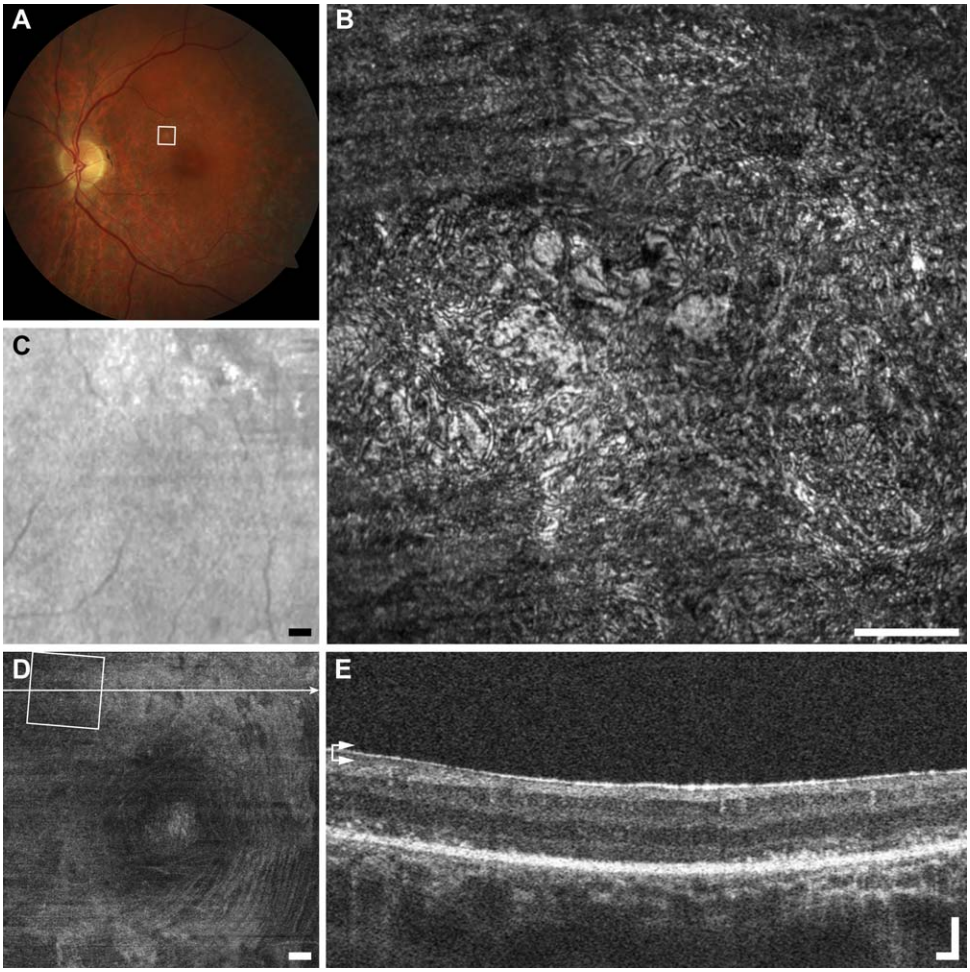

Figure 9. Multimodal imaging of waxy membrane example (**D1**), cone dystrophy KS_1154. (**A**) Fundus photo shows a yellowish membrane in the region within the region of AOSLO imaging. (**B**) The AOSLO image shows a clumpy, highly reflective membrane on the surface of the retina, obscuring the NFL underneath. *Scale bar*: 100 μm. (**C**) A SLO fundus image shows a highly reflective membrane covering a large portion of the superior portion of the image field. *Scale bar*: 200 μm. (**D**) En face OCT segmented at the level of the ILM (*horizontal arrows*) also resolves the extensive hyper-reflective membrane. *Scale bar*: 200 μm. (**E**) The OCT B-scan shows a thick hyper-reflective membrane on the surface of the NFL. *Scale bar*: 100 μm.

These features are believed by us and others (Burns SA, et al. *IOVS* 2008;49:ARVO E-Abstract 4512) to be the Gunn's dots, described in direct ophthalmoscopy and sometimes visible in fundus photography.[38,39] Unfortunately, the true identity of Gunn's dots remains to be elucidated. It has been suggested that Gunn's dots are found most easily in younger volunteers, above and below the optic nerve head (ONH) in areas of the thickest NFL. Our limited data set supports this statement (Fig. 1), and also shows these larger round reflective structures in areas of NFL disease or loss. Figures 1B2 and 1B4 show these structures in glaucoma and multiple sclerosis, both more than 12° temporal to the ONH. It is uncertain whether the Gunn's dots relocated, or were revealed by the pathologic NFL thinning. No detectable changes were observed in the appearance, location, and number of Gunn's dots in normal subjects over 2.5 months between imaging sessions, as illustrated by the images in Figure 6.

The size and distribution of Gunn's dots are inconsistent with glial cell endfeet as has been hypothesized (Burns SA, et al. *IOVS* 2008;49:ARVO E-Abstract 4512), which should be found across the entire retina in a contiguous mosaic. It is unlikely that the reflection is due to a retinal cell, since to our knowledge no glial cell or neuron has been described anterior to the ILM in the absence of disease. The size of the structures and scattered distribution around the ONH anterior to the ILM is most consistent with hyalocytes.[40] These resident macrophages of the vitreous normally are dormant, but have been implicated in the formation of epiretinal membranes.[41,42] It is hypothesized that they collect at the ONH, as well as the ciliary body, due to firm attachment of the vitreous fibers at these locations.[40]

Granular Membrane

Previous AOSLO imaging of inner retinal membranes, (Scoles DH, et al. *IOVS* 2012;53:ARVO E-Abstract 6957; Gast TJ, et al. *IOVS* 2013;54:ARVO E-Abstract 1507) found that they are common with advancing age and partial or full posterior vitreous detachment. In agreement with our findings, Gast et al. noted that these membranes are not always visualized with fundus photography and OCT. Here, we divide these hyper-reflective membranes into granular and waxy, based on appearance.

The granular membranes (Figs. 1C1–C4) appear to be composed of many small bright granules that are connected by a thin dimmer mesh-like structure, which does not obscure the underlying nerve fiber layer, or vasculature from view. The appearance is somewhat similar to the punctate features

Investigative Ophthalmology & Visual Science

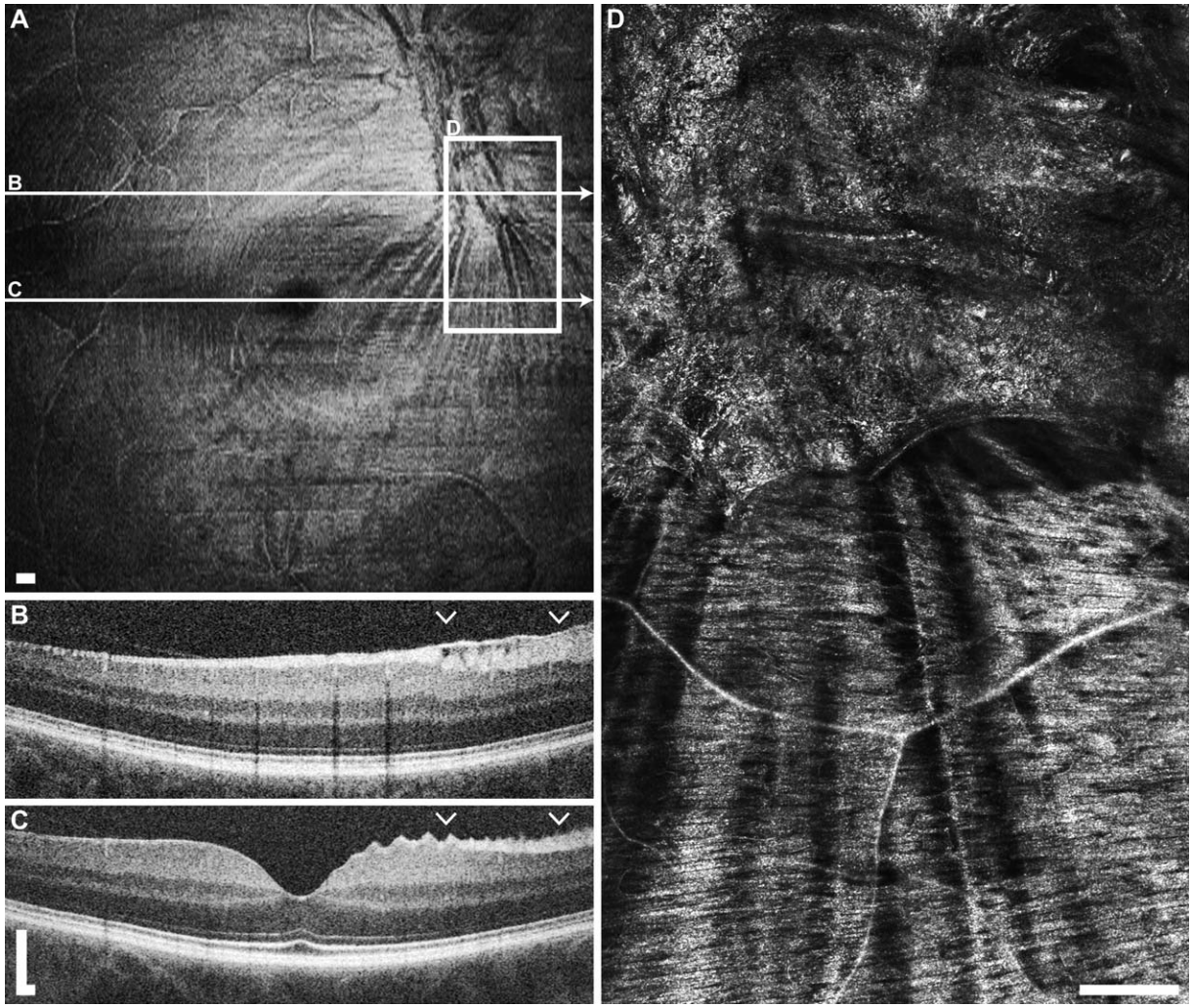

Figure 10. Example of waxy membrane with notable contraction in normal subject JC_10146 OD. (**A**) En face OCT segmented at the level of the ILM shows a hyper-reflective membrane and contraction lines superonasal to the foveal pit. (**B**) The OCT B-scan through the membrane shows a hyper-reflective layer at the ILM spanning over the NFL. *Arrowheads* indicate extent of AOSLO imaging shown in (**D**). (**C**) An OCT B-scan outside of the membrane shows an abnormal peaked appearance to the NFL. (**D**) The AOSLO imaging on and below the membrane shows the clumped waxy appearance of the membrane, as well as the linear radial shadowing in the NFL caused by the contraction of the membrane. *Scale bars*: 200 μm.

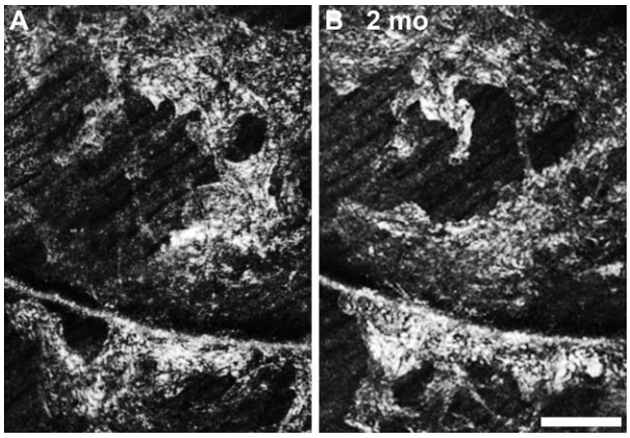

Figure 11. Two month follow up of a waxy membrane in a glaucoma patient (DLAB_0029). Despite the absence of contractile membrane (see Fig. 10), the membrane has changed in appearance significantly over a short period. *Scale bar*: 100 μm.

described above, but in these membranes no isolated puncta can be observed. These structures often are formed by two or more disconnected areas with smooth or irregular (jagged) boundaries. These membranes often contain hyporeflective areas through which the NFL and vessels are visualized. They show no obvious spatial correlation with NFL bundles, but might be somewhat related to vasculature.

We have not yet observed this type of membrane in the presence of retinal traction. In the case highlighted in Figure 7, the membrane is visualized in every modality albeit faintly. Although the membrane appears colocalized with a vessel, the OCT B-scan confirms that the hyper-reflectivity is epiretinal as opposed to adherent to the vessel itself, which is posterior to the NFL.

Waxy Membrane

In contrast to the granular hyper-reflectivity, the second category of large epiretinal finding (>50 μm across) is substantially more reflective than the other structures reported in this work, and has a smoother texture. We have termed this

Investigative Ophthalmology & Visual Science

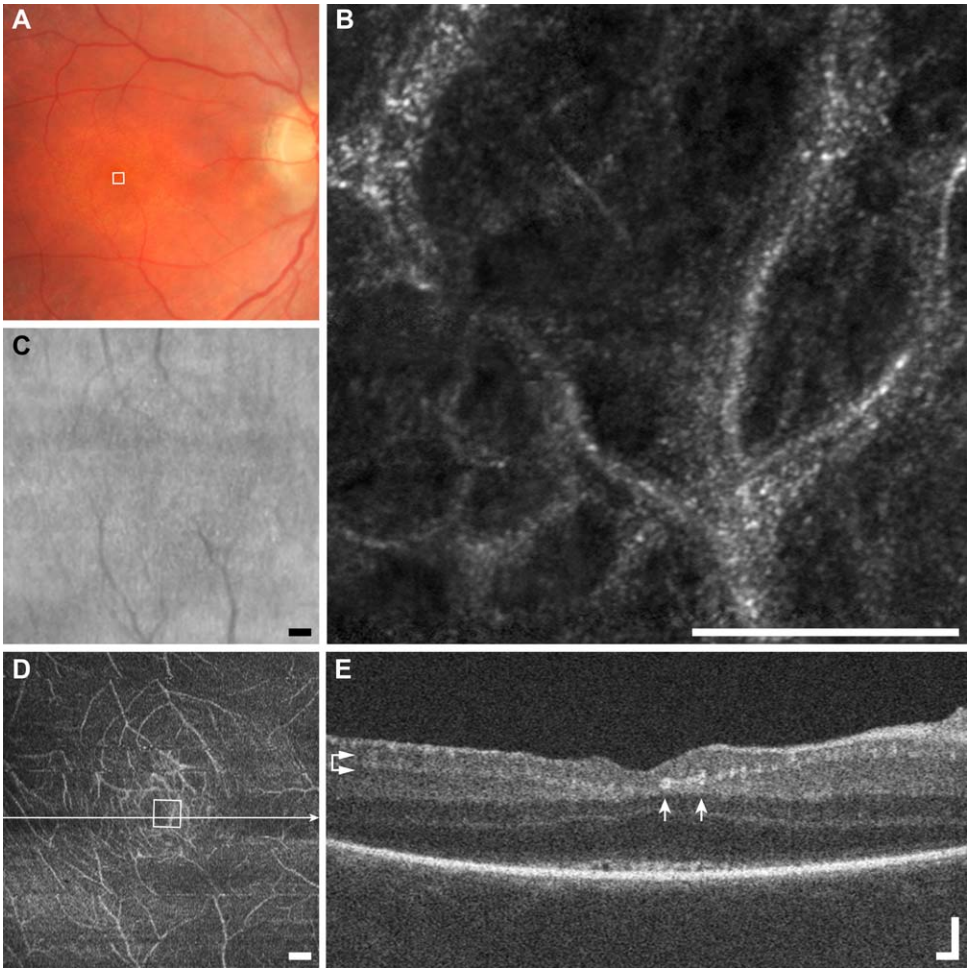

Figure 12. Multimodal imaging of vessel-associated membrane example (**E1**), Leber's congenital amaurosis JC_0579. (**A**) Fundus photo appears normal. (**B**) An AOSLO image shows capillary loops entirely coated with a hyper-reflective membrane. *Scale bar*: 100 μm. (**C**) The SLO fundus image shows no obvious pathologic changes. *Scale bar*: 200 μm. (**D**) En face OCT segmented at the level of the GCL (*horizontal arrows*) shows hyper-reflective and disorganized vasculature. *Scale bar*: 200 μm. (**E**) The OCT B-scan shows many hyper-reflective spots (*arrows*), corresponding to hyper-reflective vessels. *Scale bar*: 100 μm.

category waxy reflectivity, to evoke the appearance of candle wax dripped on a flat surface, not to imply that the composition of the structure itself is substantially different than the granular membrane. These structures obscure the underlying tissue, yet often exhibit several abrupt circular clearings within their area (Figs. 1D2, 1D3). In contrast to all other structures described here, waxy membranes appear to generate a strong specular reflection in addition to scattering incident light. An example of a normal specular reflection in the retina is the foveal reflex, visible with ophthalmoscopy, fundus photography, SLO, and OCT. This bright scintillating reflex is caused by the near perpendicular orientation of the foveal pit to the incident beam, which acts like a mirror. Waxy membranes behave similarly, and show dramatic brightness changes with retinal movements as small as 52 μm (Fig. 8), which is consistent with a specular reflection.

Some very large membranes on the surface of the NFL are visualized clearly with all imaging modalities used in this study (Fig. 9). We have found these membranes only anterior to the NFL and often in subjects with what would likely be clinically diagnosed as epiretinal membrane. Membrane traction has been noted in some eyes with these lesions, but not all. An example of a contractile waxy membrane in an asymptomatic subject is shown in Figure 10. The AO image shows the transition from a brightly reflective membrane that obscures the underlying tissue at the top to clear NFL bundles at the bottom that appear to undulate in reflectivity due to the topography of the contracted retina.

The dramatic reflectivity of these structures suggests a potential connective tissue component.[43] In agreement with previous work (Gast TJ, et al. *IOVS* 2013;54:ARVO E-Abstract 1507) we found that these membranes can remodel significantly over only 2 months (Fig. 11). Despite our categorization of these membrane-like lesions into two groups based on texture, we do not believe that we have enough evidence to perform a comparison of the granular and waxy membranes against the classical clinically described cellophane macular reflex (CMR) and preretinal macular fibrosis (PMF).[44]

Vessel-Associated Membrane

In some retinal diseases, striking hyper-reflective membranes are present in close association with retinal blood vessels. The width of these membranes in the AOSLO image varies substantially even within a small retinal area and can be as wide as four times the vessel diameter. The composition of the membranes appears to be granular structures close to or below the AOSLO diffraction limit at the wavelengths used for

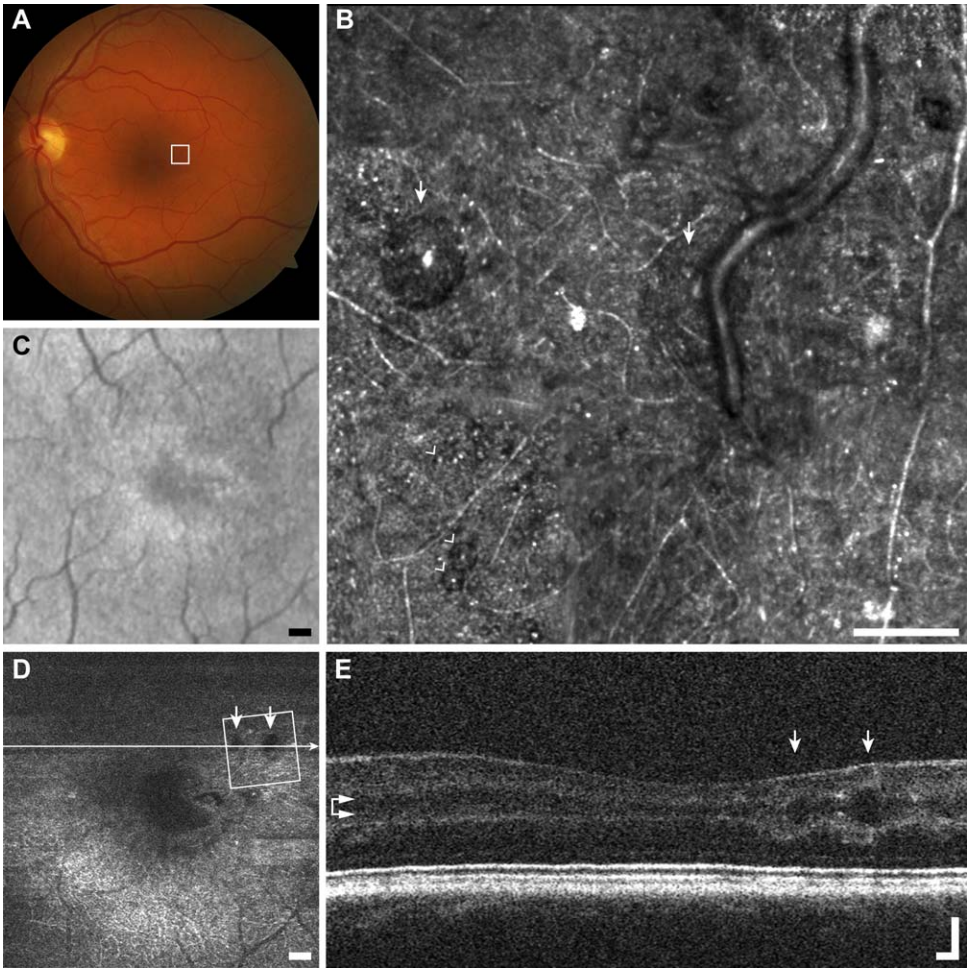

FIGURE 13. Multimodal imaging of microcysts example (**F1**), macular telangiectasia subject JC_10075. (**A**) Fundus photo does not resolve microcysts. (**B**) The AOSLO image shows a scattered distribution of very small (*arrowheads*) to very large microcysts (*arrows*). *Scale bar*: 100 μm. The borders of the cysts appear darker than the surrounding structure, and nearly all have a bright reflex on their apex. (**C**) The SLO fundus image shows disordered reflectivity, but no microcysts. *Scale bar*: 200 μm. (**D**) En face OCT segmented at the level of the INL (*horizontal arrows*) resolves only the largest microcysts (*arrows*). *Scale bar*: 200 μm. (**E**) The OCT B-scan shows the same two very large microcysts (*arrows*) seen in AOSLO imaging. *Scale bar*: 100 μm.

imaging. In contrast to the membranes described earlier, these vessel coatings reside just posterior to the NFL as shown by OCT B-scans. In Leber's congenital amaurosis, it has been shown that some genotypes have inflammatory and glial proliferations surrounding the vessels,[45] consistent with the findings in Figure 12.

Microcysts

Retinal diseases with profound inner retina cell loss, such as glaucoma and optic atrophy, sometimes can lead to microcystic spaces in the inner nuclear layer (INL).[46-48] AOSLO imaging reveals these INL microcysts with sharp distinct edges,[24] allowing for quantification and monitoring of numbers and size (Roorda A, et al. *IOVS* 2013;54:ARVO E-Abstract 3606). The shape of the microcysts ranges from round to ovoid and from 10 to 140 μm across the longest dimension. Interestingly, these cysts can act as lenses or obstructions that affect the imaging of the photoreceptors in their geometrical shadow[49] (Fig. 2F4), by altering the image magnification, brightness, or focus.

Numerous microcysts were seen in a subject with macular telangiectasia (Fig. 13). The large cysts are easily visualized with en face OCT and AOSLO, but are not resolved by LSO and fundus photography due to poor spatial sampling and the optical blur introduced by the monochromatic aberrations of the eye. Microcysts in a subject with dominant optic atrophy were found to remain relatively unchanged over 13 months (Fig. 14), in contrast to the dynamic structures highlighted above.

Striate Reflectivity

The final feature shown here in inner-retinal AOSLO imaging presents as fine hyper-reflective striae that run near perpendicular to the course of NFL axon bundles (Figs. 2G1–G4). The striations in our limited sample population extend longer than 400 μm, with average separation of 13, 11, 6, and 14 μm respectively for the examples shown in Figures 2G1 to 2G4. This feature has been noted only within the central 10° around fixation, in very limited regions. Diseases that alter the normal laminar arrangement of the retinal layers can enhance the backscattering of the Henle fiber layer,[50] a possible source of the striate hyper-reflectivity reported here. In fact, there is spatial registration between the Henle fiber reflectance in OCT and AOSLO (Fig. 15). Although not an inner retinal layer, it is possible that the Henle fiber layer is visualized with AOSLO at

Investigative Ophthalmology & Visual Science

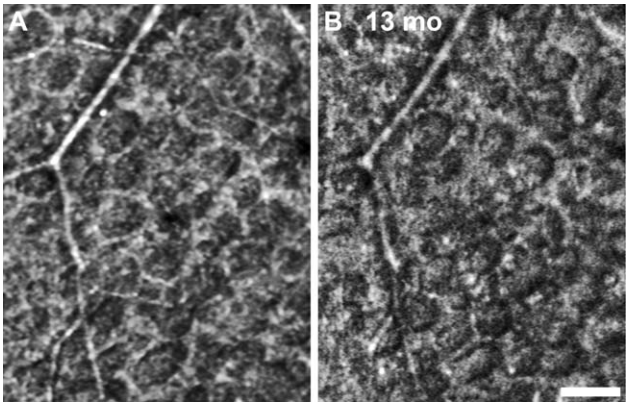

Figure 14. A 13-month follow-up of microcysts found in subject KS_1100 with dominant optic atrophy, showing no obvious changes in numbers or appearance. *Scale bar*: 50 μm.

the NFL focus in the parafovea due to the decreased separation of the layers. In addition to the striations consistent with Henle fibers (Figs. 2G1, 2G2, 2G4), we have observed striate hyper-reflectivity that does not seem related to Henle fibers (Fig. 2G3). Although these two phenomena are unlikely to be caused by the same cellular processes, their phenotypic appearance is similar and could be confused.

Discussion

A diverse set of inner and epiretinal structures that appear hyper-reflective in reflectance confocal AOSLO in various ocular and neurological conditions were observed and we propose here a classification based on qualitative appearance. We envisage that this tentative and nonexhaustive classification scheme will be expanded and refined as more eyes with disease and normal volunteers are imaged. Longitudinal confocal AOSLO studies and additional imaging modalities that provide complementary structural or functional information might provide information on the etiology of these hyper-reflective structures.

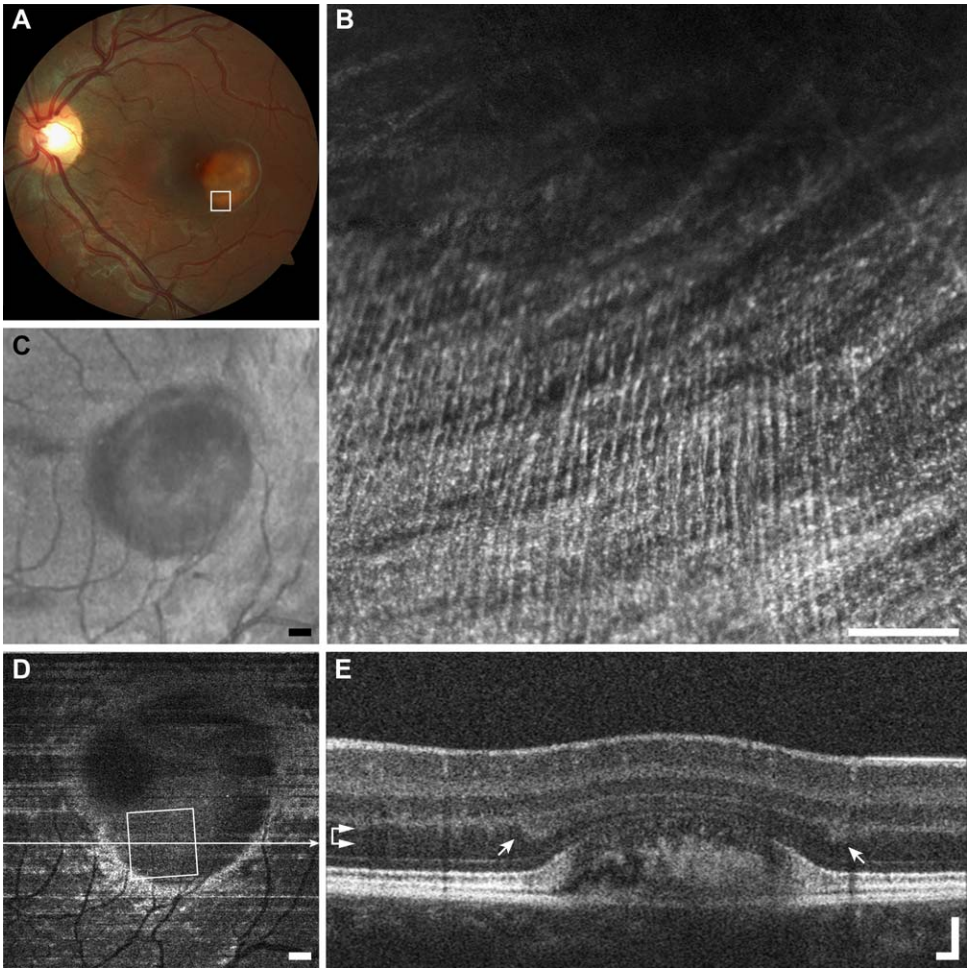

Figure 15. Multimodal imaging of striate reflectivity example (**G1**), Best's disease KS_0601. (**A**) Fundus photo shows the large vitelliform lesion just temporal to the macula. (**B**) The AOSLO image shows the NFL coursing horizontally, while a striped reflective structure runs from vertically. *Scale bar*: 100 μm. (**C**) The SLO fundus image also resolves the vitelliform lesion, but not the vertically oriented fibers. *Scale bar*: 200 μm. (**D**) En face OCT segmented along the contour of the Henle fiber layer (*horizontal arrows*) shows a rim of bright Henle fiber reflectivity surrounding the vitelliform lesion. *Scale bar*: 200 μm. (**E**) The OCT B-scan shows regions of increased Henle fiber reflection on either side of the vitelliform lesion (*arrows*). *Scale bar*: 100 μm.

Arguably, the most important finding of this study is the nonspecificity of all the reported structures when looked at only with reflectance confocal AOSLO. This strongly indicates that thorough characterization is needed before drawing conclusions and assigning causation to any given pathology. Similar to AOSLO studies reporting dark cones[10] and microaneurysms,[22] the same microscopic changes in the retina can arise due to quite different insults. The similarity of the hyperreflective features on a cellular scale across such extremely varied conditions as found in this study suggests that they are more likely caused by common downstream response pathways, rather than representing distinct disease entities. While the low specificity of any given hyper-reflective structure to a disease potentially limits the clinical applicability of confocal AOSLO imaging as a diagnostic tool, the potentially high sensitivity may provide insight on disease progression and aid management.

Although wide-reaching across conditions, this study is limited to only a few subjects per conditions. For this reason, it is not possible to report on a complete correlation of inner retinal pathology and disease. It is quite possible that each condition might have a specific retinal locus where these features first appear, or that the feature size may correlate with severity, but these questions cannot be addressed with the limited data here. Another limitation of this study is the difficulty of panretinal imaging with current AOSLO technology. Current hardware limitations prevent covering large retinal areas at multiple retinal depths in time scales comparable to current clinical tests, such as visual fields, although recent work has begun to address this limitation.[25,51] Finally, due to the retrospective nature of the analysis, we could not target any specific lesion for extensive hyperreflective structure coverage.

As new AOSLO imaging modalities are developed, it is important to re-evaluate inner and outer retinal findings, to refine this classification. For example, nonconfocal techniques implemented in commercial SLO have been shown to enhance the appearance of structures that disrupt the laminar arrangement of the retina.[52,53] Our group and others have applied these and other nonconfocal imaging to the study of the retinal pigment epithelium,[54] and retinal vasculature,[19,21,23,55] but only in a small number of subjects. Another possibility would be to exploit optical differences of each feature by adopting techniques, such as polarization sensitive imaging,[56,57] or multiple illumination wavelengths.[58,59] Regardless of imaging method advancement, analysis of microscopic changes should include a variety of patients to gain a greater appreciation for the specificity of findings. The data presented here serve as a useful starting point for future studies examining the inner retina with AOSLO.

Acknowledgments

The authors thank Yusufu N. Sulai, Christopher Langlo, Mara Goldberg, William J. Wirostko, Bernd F. Remler, Dennis P. Han, Ryan D. Walsh, Sang H. Hong, Scott Robison, Wanda M. Martinez, Shakeel Shareef, Gerald A. Fishman, Thomas B. Connor Jr, Deborah M. Costakos, and Ravi S. Singh for contributions to the preparation of this manuscript.

Presented in part at the annual meeting of the Association for Research in Vision and Ophthalmology, Seattle, Washington, May 5–9, 2013 (Scoles DH, et al. *IOVS* 2013;54:ARVO E-Abstract 1434).

Supported by National Institutes of Health (NIH) Grants R01EY017607, P30EY001931, UL1TR000055, and T32GM007356, by a Career Development Award from Research to Prevent Blindness (RPB) and a Career Award at the Scientific Interface from the Burroughs Wellcome Fund (AD), and by grants from the Foundation Fighting Blindness, RD & Linda Peters Foundation, Fight for Sight, an unrestricted departmental grant from RPB, and the Glaucoma Research Foundation Catalyst for a Cure Initiative. This investigation was conducted in a facility constructed with support from the Research Facilities Improvement Program and Grant C06-RR016511 from the National Center for Research Resources, NIH. The authors alone are responsible for the content and writing of the paper.

Disclosure: **D. Scoles**, None; **B.P. Higgins**, None; **R.F. Cooper**, None; **A.M. Dubis**, None; **P. Summerfelt**, None; **D.V. Weinberg**, None; **J.E. Kim**, Allergan (C); **K.E. Stepien**, None; **J. Carroll**, None; **A. Dubra**, None

References

1. Liang J, Williams DR, Miller DT. Supernormal vision and high-resolution retinal imaging through adaptive optics. *J Opt Soc Am A*. 1997;14:2884–2892.
2. Miller DT, Williams DR, Morris GM, Liang J. Images of cone photoreceptors in the living human eye. *Vision Res*. 1996;36:1067–1079.
3. Carroll J, Neitz M, Hofer H, Neitz J, Williams DR. Functional photoreceptor loss revealed with adaptive optics: an alternate cause of color blindness. *Proc Natl Acad Sci U S A*. 2004;101:8461–8466.
4. Carroll J, Choi SS, Williams DR. In vivo imaging of the photoreceptor mosaic of a rod monochromat. *Vision Res*. 2008;48:2564–2568.
5. Genead MA, Fishman GA, Rha J, et al. Photoreceptor structure and function in patients with congenital achromatopsia. *Invest Ophthalmol Vis Sci*. 2011;52:7298–7308.
6. Merino D, Duncan JL, Tiruveedhula P, Roorda A. Observation of cone and rod photoreceptors in normal subjects and patients using a new generation adaptive optics scanning laser ophthalmoscope. *Biomed Opt Express*. 2011;2:2189–2201.
7. Flatter J, Cooper RF, Dubow MJ, et al. Outer retinal structure following closed globe blunt ocular trauma [published online ahead of print April 18,2014]. *Retina*.
8. Kay DB, Land ME, Cooper RF, et al. Outer retinal structure in best vitelliform macular dystrophy. *JAMA Ophthalmol*. 2013;131:1207–1215.
9. Hansen SO, Cooper RF, Dubra A, Carroll J, Weinberg DV. Selective cone photoreceptor injury in acute macular neuroretinopathy. *Retina*. 2013;33:1650–1658.
10. Carroll J, Kay DB, Scoles D, Dubra A, Lombardo M. Adaptive optics retinal imaging–clinical opportunities and challenges. *Curr Eye Res*. 2013;38:709–721.
11. Zhong Z, Petrig BL, Qi X, Burns SA. In vivo measurement of erythrocyte velocity and retinal blood flow using adaptive optics scanning laser ophthalmoscopy. *Opt Express*. 2008;16:12746–12756.
12. Tam J, Martin JA, Roorda A. Noninvasive visualization and analysis of parafoveal capillaries in humans. *Invest Ophthalmol Vis Sci*. 2010;51:1691–1698.
13. Tam J, Dhamdhere KP, Tiruveedhula P, et al. Disruption of the retinal parafoveal capillary network in type 2 diabetes before the onset of diabetic retinopathy. *Invest Ophthalmol Vis Sci*. 2011;52:9257–9266.
14. Wang Q, Kocaoglu OP, Cense B, et al. Imaging retinal capillaries using ultrahigh-resolution optical coherence tomography and adaptive optics. *Invest Ophthalmol Vis Sci*. 2011;52:6292–6299.
15. Bedggood P, Metha A. Direct visualization and characterization of erythrocyte flow in human retinal capillaries. *Biomed Opt Express*. 2012;3:3264–3277.

16. Kurokawa K, Sasaki K, Makita S, Hong YJ, Yasuno Y. Three-dimensional retinal and choroidal capillary imaging by power Doppler optical coherence angiography with adaptive optics. *Opt Express*. 2012;20:22796–22812.
17. Dubis AM, Hansen BR, Cooper RF, Beringer J, Dubra A, Carroll J. Relationship between the foveal avascular zone and foveal pit morphology. *Invest Ophthalmol Vis Sci*. 2012;53:1628–1636.
18. Chui TY, Zhong Z, Song H, Burns SA. Foveal avascular zone and its relationship to foveal pit shape. *Optom Vis Sci*. 2012; 89:602–610.
19. Chui TY, Vannasdale DA, Burns SA. The use of forward scatter to improve retinal vascular imaging with an adaptive optics scanning laser ophthalmoscope. *Biomed Opt Express*. 2012;3: 2537–2549.
20. Tam J, Dhamdhere KP, Tiruveedhula P, et al. Subclinical capillary changes in non-proliferative diabetic retinopathy. *Optom Vis Sci*. 2012;89:E692–703.
21. Burns SA, Elsner AE, Chui TY, et al. In vivo adaptive optics microvascular imaging in diabetic patients without clinically severe diabetic retinopathy. *Biomed Opt Express*. 2014;5:961–974.
22. Dubow M, Pinhas A, Shah N, et al. Classification of human retinal microaneurysms using adaptive optics scanning light ophthalmoscope fluorescein angiography. *Invest Ophthalmol Vis Sci*. 2014;55:1299–1309.
23. Sulai YN, Scoles D, Harvey Z, Dubra A. Visualization of retinal vascular structure and perfusion with a nonconfocal adaptive optics scanning light ophthalmoscope. *J Opt Soc Am A*. 2014; 31:569–579.
24. Gocho K, Kikuchi S, Kabuto T, et al. High-resolution en face images of microcystic macular edema in patients with autosomal dominant optic atrophy. *Biomed Res Int*. 2013; 2013:676803.
25. Huang G, Qi X, Chui TY, Zhong Z, Burns SA. A clinical planning module for adaptive optics SLO imaging. *Optom Vis Sci*. 2012;89:593–601.
26. Takayama K, Ooto S, Hangai M, et al. High-resolution imaging of retinal nerve fiber bundles in glaucoma using adaptive optics scanning laser ophthalmoscopy. *Am J Ophthalmol*. 2013;155:870–881.
27. Takayama K, Ooto S, Hangai M, et al. High-resolution imaging of the retinal nerve fiber layer in normal eyes using adaptive optics scanning laser ophthalmoscopy. *PLoS One*. 2012;7: e33158.
28. Lombardo M, Scarinci F, Ripandelli G, Cupo G, Stirpe M, Serrao S. Adaptive optics imaging of idiopathic epiretinal membranes. *Ophthalmology*. 2013;120:1508–1509. e1501.
29. Hirsch J, Curcio CA. The spatial resolution capacity of human foveal retina. *Vision Res*. 1989;29:1095–1101.
30. Tanna H, Dubis AM, Ayub N, et al. Retinal imaging using commercial broadband optical coherence tomography. *Br J Ophthalmol*. 2010;94:372–376.
31. Dubra A, Sulai Y. Reflective afocal broadband adaptive optics scanning ophthalmoscope. *Biomed Opt Express*. 2011;2: 1757–1768.
32. ANSI. *American National Standard for Safe Use of Lasers in Research, Development, or Testing*. Orlando, FL: Laser Institute of America; 2007.
33. Delori FC, Webb RH, Sliney DH. Maximum permissible exposures for ocular safety (ANSI 2000), with emphasis on ophthalmic devices. *J Opt Soc Am A*. 2007;24:1250–1265.
34. Wilson T, Carlini AR. Size of the detector in confocal imaging systems. *Optics Letters*. 1987;12:227–229.
35. Dubra A, Harvey Z. *Registration of 2D Images from Fast Scanning Ophthalmic Instruments. The 4th International Workshop on Biomedical Image Registration*. Lübeck, Germany: Springer-Verlag; 2010:60–71.
36. Li ZY, Possin DE, Milam AH. Histopathology of bone spicule pigmentation in retinitis pigmentosa. *Ophthalmology*. 1995; 102:805–816.
37. Feeney L. Lipofuscin and melanin of human retinal pigment epithelium. Fluorescence, enzyme cytochemical, and ultrastructural studies. *Invest Ophthalmol Vis Sci*. 1978;17:583–600.
38. Gunn RM, Schafer EAA. Contribution to the minute anatomy of the human retina. *J Anat Physiol*. 1877;11:357–516.
39. Ballantyne AJ. The reflexes of the fundus oculi: (section of ophthalmology). *Proc R Soc Med*. 1940;34:19–42.
40. Sakamoto T, Ishibashi T. Hyalocytes: essential cells of the vitreous cavity in vitreoretinal pathophysiology? *Retina*. 2011; 31:222–228.
41. Kohno RI, Hata Y, Kawahara S, et al. Possible contribution of hyalocytes to idiopathic epiretinal membrane formation and its contraction. *Br J Ophthalmol*. 2009;93:1020–1026.
42. Schumann RG, Eibl KH, Zhao F, et al. Immunocytochemical and ultrastructural evidence of glial cells and hyalocytes in internal limiting membrane specimens of idiopathic macular holes. *Invest Ophthalmol Vis Sci*. 2011;52:7822–7834.
43. Oberstein SY, Byun J, Herrera D, Chapin EA, Fisher SK, Lewis GP. Cell proliferation in human epiretinal membranes: characterization of cell types and correlation with disease condition and duration. *Mol Vis*. 2011;17:1794–1805.
44. Klein R, Klein BE, Wang Q, Moss SE. The epidemiology of epiretinal membranes. *Trans Am Ophthalmol Soc*. 1994;92: 403–425, discussion 425–430.
45. Heegaard S, Rosenberg T, Preising M, Prause JU, Bek T. An unusual retinal vascular morphology in connection with a novel AIPL1 mutation in Leber's congenital amaurosis. *Br J Ophthalmol*. 2003;87:980–983.
46. Gills JP Jr, Wadsworth JA. Degeneration of the inner nuclear layer of the retina following lesions of the optic nerve. *Trans Am Ophthalmol Soc*. 1966;64:66–88.
47. Gelfand JM, Nolan R, Schwartz DM, Graves J, Green AJ. Microcystic macular oedema in multiple sclerosis is associated with disease severity. *Brain*. 2012;135:1786–1793.
48. Burggraaff MC, Trieu J, de Vries-Knoppert WA, Balk L, Petzold A. The clinical spectrum of microcystic macular edema. *Invest Ophthalmol Vis Sci*. 2014;55:952–961.
49. Langlo CS, Flatter JA, Dubra A, Wirostko WJ, Carroll J. A lensing effect of inner retinal cysts on images of the photoreceptor mosaic. *Retina*. 2014;34:421–422.
50. Lujan BJ, Roorda A, Knighton RW, Carroll J. Revealing Henle's fiber layer using spectral domain optical coherence tomography. *Invest Ophthalmol Vis Sci*. 2011;52:1486–1492.
51. Dubra A, Sulai YN. First-order design of a reflective viewfinder for adaptive optics ophthalmoscopy. *Opt Express*. 2012;20: 26596–26605.
52. Shin YU, Lee BR. Retro-mode imaging for retinal pigment epithelium alterations in central serous chorioretinopathy. *Am J Ophthalmol*. 2012;154:155–163.
53. Yamamoto M, Mizukami S, Tsujikawa A, Miyoshi N, Yoshimura N. Visualization of cystoid macular oedema using a scanning laser ophthalmoscope in the retro-mode. *Clin Experiment Ophthalmol*. 2010;38:27–36.
54. Scoles D, Sulai YN, Dubra A. In vivo dark-field imaging of the retinal pigment epithelium cell mosaic. *Biomed Opt Express*. 2013;4:1710–1723.
55. Chui TY, Gast TJ, Burns SA. Imaging of vascular wall fine structure in the human retina using adaptive optics scanning laser ophthalmoscopy. *Invest Ophthalmol Vis Sci*. 2013;54: 7115–7124.

Investigative Ophthalmology & Visual Science

56. Pircher M, Hitzenberger CK, Schmidt-Erfurth U. Polarization sensitive optical coherence tomography in the human eye. *Prog Retin Eye Res*. 2011;30:431–451.

57. Song H, Qi X, Zou W, Zhong Z, Burns SA. Dual electro-optical modulator polarimeter based on adaptive optics scanning laser ophthalmoscope. *Opt Express*. 2010;18:21892–21904.

58. Grieve K, Tiruveedhula P, Zhang Y, Roorda A. Multi-wavelength imaging with the adaptive optics scanning laser ophthalmoscope. *Opt Express*. 2006;14:12230–12242.

59. Dubra A, Sulai Y, Norris JL, et al. Noninvasive imaging of the human rod photoreceptor mosaic using a confocal adaptive optics scanning ophthalmoscope. *Biomed Opt Express*. 2011; 2:1864–1876.

Investigative Ophthalmology & Visual Science